



# Study of aerosol optical properties at Kunming in southwest China and long-range transport of biomass burning aerosols from North Burma



J. Zhu<sup>a,d,e</sup>, X. Xia<sup>a,b,\*</sup>, H. Che<sup>c</sup>, J. Wang<sup>d</sup>, J. Zhang<sup>a,b</sup>, Y. Duan<sup>f</sup>

<sup>a</sup> LAGEO, Institute of Atmospheric Physics, Chinese Academy of Sciences, Beijing 100029, China

<sup>b</sup> Collaborative Innovation Center on Forecast and Evaluation of Meteorological Disasters, Nanjing University of Information Science & Technology, Nanjing 210044, China

<sup>c</sup> LAC, Chinese Academy of Meteorological Sciences, Beijing 100081, China

<sup>d</sup> Department of Earth and Atmospheric Sciences, University of Nebraska—Lincoln, Lincoln, NE, USA

<sup>e</sup> University of Chinese Academy of Sciences, Beijing 100049, China

<sup>f</sup> Fuming Meteorological Bureau, Kunming, China

## ARTICLE INFO

### Article history:

Received 25 March 2015

Received in revised form 13 October 2015

Accepted 13 October 2015

Available online 22 October 2015

### Keywords:

Aerosol optical properties

Aerosol type and source

Long-range transport

## ABSTRACT

Seasonal variation of aerosol optical properties and dominant aerosol types at Kunming (KM), an urban site in southwest China, is characterized. Substantial influences of the hygroscopic growth and long-range transport of biomass burning (BB) aerosols on aerosol optical properties at KM are revealed. These results are derived from a detailed analysis of (a) aerosol optical properties (e.g. aerosol optical depth (AOD), columnar water vapor (CWV), single scattering albedo (SSA) and size distribution) retrieved from sunphotometer measurements during March 2012–August 2013, (b) satellite AOD and active fire products, (c) the attenuated backscatter profiles from the space-borne lidar, and (d) the back-trajectories. The mean  $AOD_{440nm}$  and extinction Angstrom exponent ( $EAE_{440-870}$ ) at KM are  $0.42 \pm 0.32$  and  $1.25 \pm 0.35$ , respectively. Seasonally, high  $AOD_{440nm}$  ( $0.51 \pm 0.34$ ), low  $EAE_{440-870}$  ( $1.06 \pm 0.34$ ) and high CWV ( $4.25 \pm 0.97$  cm) during the wet season (May–October) contrast with their counterparts  $0.17 \pm 0.11$ ,  $1.40 \pm 0.31$  and  $1.91 \pm 0.37$  cm during the major dry season (November–February) and  $0.53 \pm 0.29$ ,  $1.39 \pm 0.19$ , and  $2.66 \pm 0.44$  cm in the late dry season (March–April). These contrasts between wet and major dry season, together with the finding that the fine mode radius increases significantly with AOD during the wet season, suggest the importance of the aerosol hygroscopic growth in regulating the seasonal variation of aerosol properties. BB and Urban/Industrial (UI) aerosols are two major aerosol types. Back trajectory analysis shows that airflows on clean days during the major dry season are often from west of KM where the AOD is low. In contrast, air masses on polluted days are from west (in late dry season) and east (in wet season) of KM where the AOD is often large. BB air mass is found mostly originated from North Burma where BB aerosols are lifted upward to 5 km and then subsequently transported to southwest China via prevailing westerly winds.

© 2015 Elsevier B.V. All rights reserved.

## 1. Introduction

Atmospheric aerosols from natural and anthropogenic sources have important impacts on climate, air quality and human health. To understand these impacts, it is essential to characterize aerosol optical, physical, and chemical properties at different locations because of their highly temporal variability and spatial inhomogeneity. Ground-based remote sensing of aerosols is one of the important tools in accurately characterizing column-integrated aerosol optical and physical properties. Ground-based network of remote sensing aerosol optical properties using sunphotometer goes back to 1960s in America and Europe (Volz, 1965; Holben et al., 2001 and references therein). Several

international and regional ground-based sunphotometer networks have been established during recent decades, for example, the Aerosol Robotic Network (AERONET) (Holben et al., 1998), SKYradiometer Network (Uchiyama et al., 2005), the Global Atmosphere Watch Precision Filter Radiometer network (Wehrli, 2005), and China Aerosol Remote Sensing Network (CARSNET) (Che et al., 2009). The data have been widely used by the aerosol community to characterize aerosol optical properties, to evaluate satellite retrievals and model simulations, and to study aerosol effects on climate (Holben et al., 2001).

Column-integrated aerosol optical and physical properties based on ground-based remote sensing data were widely studied in east China (Xia et al., 2007), the North China Plain (Che et al., 2014; Xia et al., 2005) and the Tibetan Plateau (Huang et al., 2007; Li et al., 2011 and references therein). Xia et al. (2005) showed that the monthly mean aerosol optical depth (AOD) at 750 nm in spring could range from 0.32 to 0.68 in North China. In the urban region of North China Plain, AOD

\* Corresponding author at: LAGEO, Institute of Atmospheric Physics, CAS, China.

Tel.: +86 10 82995071; fax: +86 10 82995073.

E-mail address: [xxa@mail.iap.ac.cn](mailto:xxa@mail.iap.ac.cn) (X. Xia).

seasonal variation can be more distinct and the annual mean AOD at 550 nm can reach 0.8 (Li et al., 2007). Equally high values of the annual mean AOD were also observed over south China, such as 0.7 in the Sichuan Basin (Luo et al., 2001; Tao et al., 2013). While the atmosphere over the Tibetan Plateau is pristine in general, it can be occasionally affected by long-range transport of dust aerosols from the Taklimakan Desert in summer and anthropogenic aerosols from South Asia in spring (Huang et al., 2007; Xia et al., 2008). However, the study of ground-based remote sensing of aerosol optical properties in southwest China is still quite limited.

It is expected that aerosol properties in southwest China should be quite different from those in other regions of China because of differences in topography, regional climate, and aerosol sources. Due to the high elevation (exceeding 1 km) and the low latitude, the climate in southwest China is characterized by a few interesting features, for example, year-long intense solar radiation and large diurnal variation, small monthly variations of temperature and the two distinct seasons, namely the wet season (May–October) which contributes 85% of the annual rainfall (Qin et al., 2010) and the dry season (November–April) with an average of 20 days of sunshine in a month. It therefore can be hypothesized that the aerosol hygroscopic process may render different aerosol properties between the dry and wet seasons.

Biomass burning (BB) in Asia is an important contributor to air pollution in the region (Streets et al., 2003; Sahu and Saxena, 2015). Many studies show its influence on regional gaseous pollutant (Zhao et al., 2015) and aerosol properties such as particle matter (PM) concentration and chemical compositions (Deka and Hoque, 2014; Wang et al., 2015). Although some studies found that aerosol and gases from BB in South and Southeast Asia can be transported to Southeast China and the northwestern Pacific (Zhang et al., 2012; Jacob et al., 2003), few studies highlighted possible impact of emission from South and Southeast Asia on air quality and regional climate in southwest China. On the basis of aerosol chemical speciation data (Hao and Liu, 1994; Streets et al., 2003), the BB aerosols from long-range transport are found in southwest China. However, the impact of such transport on the column-integrated aerosol optical properties in southwest China is limited in part due to the lack of ground-based observations. To overcome this limitation and evaluate the importance of aerosol hygroscopicity in regulating the characteristics of aerosol properties, in 2012 we have established a sunphotometer site at Kunming (KM), the capital of Yunnan Province, southwest China.

This study presents, for the first time, the ground-based sunphotometer measurements of aerosol optical properties and aerosol types at KM in southwest China, including their seasonal variations and the attribution of different processes (such as long-range transport vs. local emission and hygroscopicity) to these variations. While accurate, sunphotometer measurements are nevertheless taken at only one location (point) and hence lack spatial coverage. To tackle this challenge, a combined analysis of aerosol data from ground-based and satellite remote sensing measurements as well as the back-trajectories is conducted. The data and methods are introduced in Section 2. Sections 3 and 4 present the results of aerosol properties and process analysis, respectively. The discussion and conclusions are given in Section 5.

## 2. Site, data and methodology

### 2.1. Site

The sunphotometer site (25.01°N, 102.65°E) is located west of KM, with an elevation of 1889 m a.s.l. The instrument is established at the observation field of the Kunming Xishan district Meteorological bureau. This field is surrounded by grass and crops without serious pollution sources nearby. For the mean climate, there are two abrupt jumps of the monthly precipitation. Monthly precipitation increases dramatically from 24 cm in April to 98 cm in May and decreases from 80 cm in

October to 42 cm in November (Qin et al., 2010) that is associated with monsoon onsets in May and withdraws in October (Yan et al., 2013).

Fig. 1 shows the seasonal wind, pressure and relative humidity (RH) at surface (995 sig level) of the National Center of Environmental Prediction (NCEP) reanalysis monthly data in wet and dry seasons during 2012–2013. The southwest and southeast winds are the prevailing winds in both seasons, and the westerly wind speed is normally larger than the easterly wind. The RH is about 90% and 70% in wet and dry season, respectively. Interestingly, KM on average is at the north edge of the inter-tropical convergence zone (ITCZ) in its wet season (Fig. 1), and hence, both the emission and the transport of aerosol from the south of KM have strong seasonal variations. Since biomass burning events occurred more frequently in the late of dry season (also the transition period from dry to wet) in Southeast Asia, we further divide the period of November–April (the dry season) into the major dry (November–February: dry1) and late dry (March–April, also biomass burning period: dry2) seasons.

### 2.2. Data

#### 2.2.1. Aerosol optical properties from CE-318 sunphotometer observation

The column-integrated aerosol optical properties are derived from CE-318 sunphotometer measurements at KM from March 2012 to August 2013. Therefore, the observations in March–August are from two years, and the other months from one year. The instrument performs direct sun extinction measurements at 340, 380, 440, 500, 675, 870, 940 and 1020 nm and sky radiance measurements at 440, 675, 870, and 1020 nm (the nominal wavelength). The sun direct measurements at 340, 380, 440, 500, 675, 870 and 1020 nm wavelengths are used to calculate AODs based on Beer Law. Measurements at 940 nm are used to derive the columnar water vapor (CWV) in centimeters (Holben et al., 1998). Aerosol microphysical and optical properties like size distributions, refractive indices, and single scattering albedos (SSA) were retrieved by using sky radiance almucantar measurements and direct sun measurements following the AERONET procedures described in Dubovik and King (2000) and Dubovik et al. (2006). The cloud-screened algorithm of Smirnov et al. (2000) is adopted to produce Level 1.5 aerosol products. The suspicious Level 1.5 aerosol products are finally quality controlled using surface meteorological data.

The instrument was calibrated before and after the observation period using the calibration facility of Chinese Academy of Meteorological Sciences (Che et al., 2009; Tao et al., 2014). The sun direct calibration was made via inter-comparison with the master sunphotometers at Beijing. The master sunphotometers were calibrated using the Langley method at either the Izaña, Spain (28.31°N, 16.50°W, 2391.0 m a.s.l.) or the Mauna Loa, USA (19.54°N, 55.58°W, 3397.0 m a.s.l.) (Che et al., 2014). The sphere calibration methods and protocols for the CARSONET have been described by Tao et al. (2014). The CARSONET sphere calibration results were compared with the original values provided by the Cimel manufacturer, showing differences of ~3–5% at infrared wavelengths (1020 and 870 nm) and ±3% at visible wavelengths (440, 500, and 675 nm).

The comparison of AOD between CARSONET with AERONET in Beijing showed the difference is about 0.01 at 440 nm (Che et al., 2009), which is consistent with the expected accuracy of 0.01–0.02 for the AERONET AOD (Holben et al., 1998; Eck et al., 1999). CWV amount is retrieved with uncertainty of <10% (Holben et al., 1998). Three extinction Angstrom exponents (EAE) are calculated from spectral AOD at 440 and 870 nm ( $EAE_{440-870}$ ), from AOD at 440 and 675 nm ( $EAE_{440-675}$ ), and from AOD at 675 and 870 nm ( $EAE_{675-870}$ ) (Ångström, 1929). Similar to EAE, the absorption Angstrom exponent (AAE) is calculated from spectral absorption AOD (AAOD) at 440 nm and 870 nm. AAOD is calculated from AOD and SSA. The SSA uncertainty is estimated to be less than 0.03 for AOD at 440 nm > 0.4 and the uncertainty increases for lower AOD (Dubovik and King, 2000; Dubovik et al., 2000, 2002).

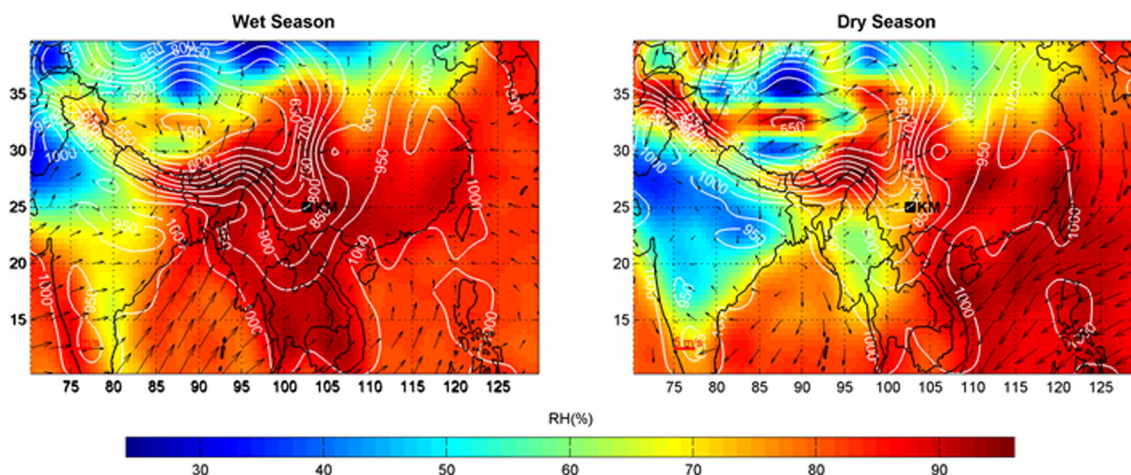


**Fig. 1.** The surface wind, pressure, and relative humidity (RH) of the wet (May–October) and dry (November–April) seasons using the NCEP/NCAR reanalysis monthly data during 2012–2013. Winds are shown with arrows pointing toward the wind’s direction, where the length of arrows defines the magnitude of wind speed (m/s), the white line contour represents pressure (mb) and shaded color contour represents RH (%). The reference wind vector of 5 m/s is the short red line located to the bottom left of the figure. (For interpretation of the references to color in this figure legend, the reader is referred to the web version of this article.)

Uncertainties of EAE and AAE are generally larger than those of AOD and SSA. The volume size distribution is fitted using two log-normal distributions and thereby nine size parameters are derived for the fine and coarse mode.

2.2.2. The MODIS AOD and fire products

The Moderate Resolution Imaging Spectroradiometer (MODIS) is an instrument onboard the Terra and Aqua satellites. The Terra and Aqua are polar-orbiting satellites that orbit the Earth in morning descending and afternoon ascending directions, respectively. The MODIS instrument collects spectral irradiance data at 36 wavelength bands ranging from 0.4 to 14.4 μm (from visible to thermal infrared) and covers the globe every 1 to 2 days.

The MODIS Collection 6 Deep-Blue/Dark-Target combined AOD data at 550 nm (Levy et al., 2013) (MODIS\_AOD) with spatial resolution of 10 × 10 km from 2012 to 2013 are used to characterize the spatial-temporal variation of aerosol loading in southwest China and its surrounding areas. The MODIS\_AOD have been validated using global AEORNET aerosol products (Levy et al., 2010, 2013). Comparison of the Terra and Aqua MODIS collection 6 Deep-Blue/Dark-Target combined AOD with sunphotometer AOD at KM is shown in Fig. 2. In the comparison, the CIMEL AODs were averaged in time (±0.5 h of MODIS overpasses) and MODIS\_AODs were averaged in space (over a 5 by 5 array of 10 km pixels centered at KM). The results show that MODIS\_AOD has a good agreement with sunphotometer observation. The mean bias is nearly zero and the percentage of data within the expected error 0.05 + 0.15AOD is 71.1%.

The MODIS monthly fire location product data (MCD14ML) were downloaded from the University of Maryland website (<ftp://fuoco.geog.umd.edu>). The data contain the Terra and Aqua MODIS fire pixels in a single monthly ASCII files. The data descriptions and validation are reported in the literature (Giglio, 2013). The fire locations with the detection confidence of 100 are used to show fire activity and its potential effects.

2.2.3. The CALIOP profile data

The Cloud–Aerosol Lidar with Orthogonal Polarization (CALIOP) instrument, onboard the Cloud–Aerosol Lidar and Infrared Pathfinder Satellite Observation (CALIPSO), provides the total backscatter coefficient profile at 532 and 1064 nm, and the linear depolarization profile at 532 nm (Winker et al., 2003). The CALIPSO level 1 attenuated

backscattering coefficient profiles at 532 nm (version 3.30) are used to show long-range transport of BB aerosols to KM.

2.2.4. The meteorological data

The NCEP reanalysis meteorological data of monthly wind, pressure, relative humidity (RH) and vertical velocity (Omega) over the research region are available on the website (<http://www.esrl.noaa.gov/>) (Kalnay et al., 1996). The spatial resolution of these data is 2.5 × 2.5°. The ground observed data of daily average RH at KM during 2012–2013 are from China Meteorological Administration (CMA).

2.3. Methodology

Three methods are applied to reveal the hygroscopic growth of aerosols during the wet season and its significant effects on aerosol

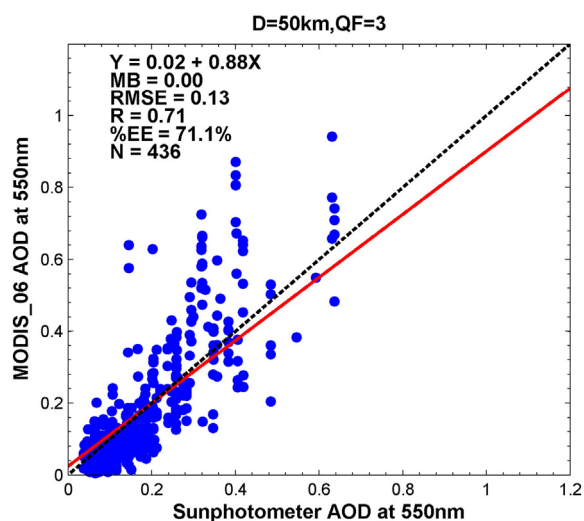


**Fig. 2.** Scatter plot of MODIS collection 6 Deep-Blue/Dark-Target combined AOD and sunphotometer derived AOD at 550 nm over KM by using spatial average of MODIS data with diameter of 50 km and time average of sunphotometer observations with plus or minus 30 min of satellite passing time. MB is the mean bias; RMSE is root mean squared error; R stands for Pearson correlation coefficient; %EE is the percentage of data within the expected error 0.05 + 0.15AOD and N is the number of matchup data of both Terra and Aqua.

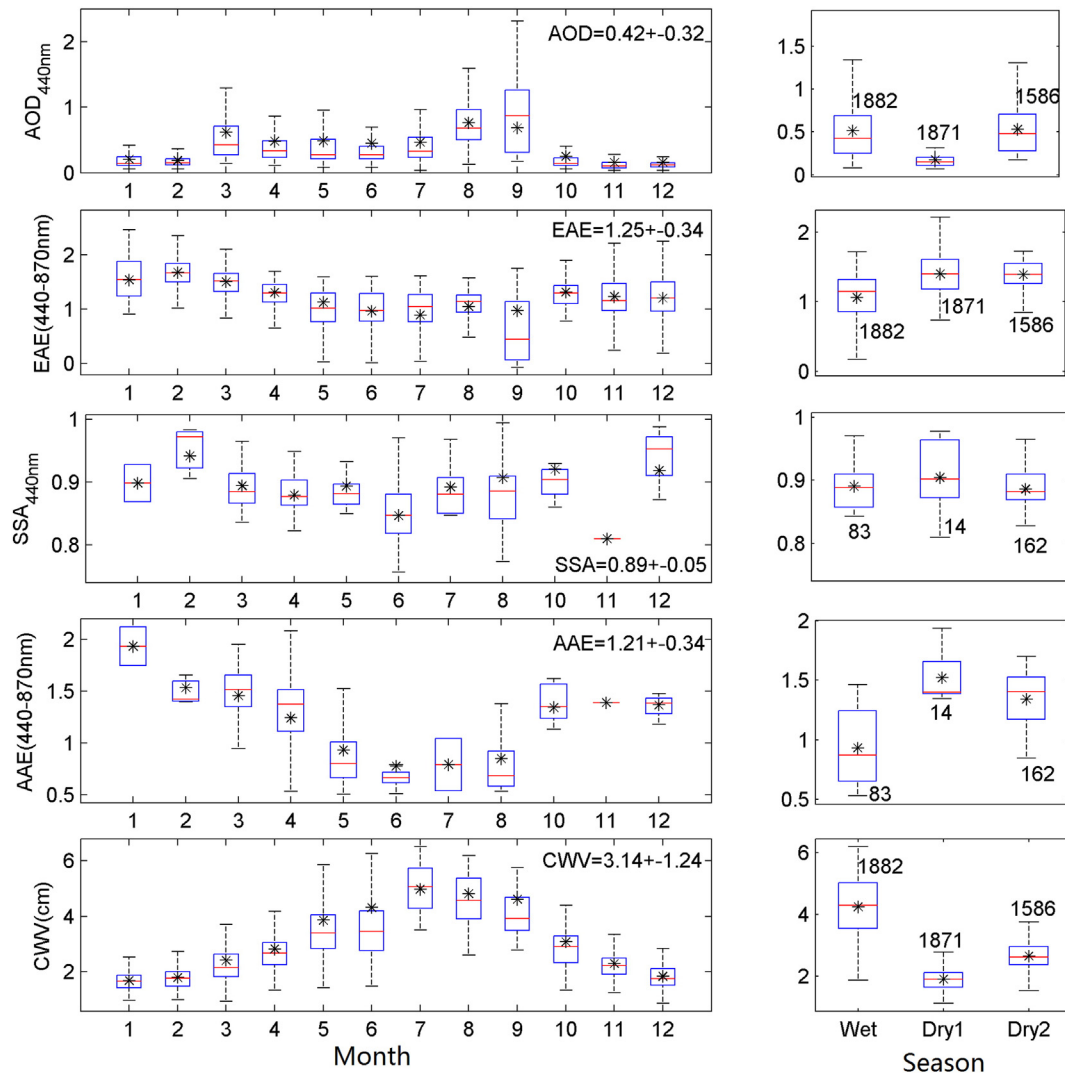


**Fig. 3.** Box plots of monthly (left) and seasonal (right) aerosol properties: aerosol optical depth (AOD), extinction Angstrom exponent (EAE), single scattering albedo (SSA), absorption Angstrom exponent (AAE), and the columnar water vapor (CWV). In each box, the central red-line is the median and the lower and upper limits are the first and the third quartiles, respectively. The lines extending vertically from the box indicate the spread of the distribution with the length being 1.5 times the difference between the first and the third quartiles. The asterisk symbols indicate the geometric means. The seasons are wet (May–October), dry1 (November–February) and dry2 (March–April) seasons respectively. The numbers beside the box corresponding to each season for different parameters are the numbers of instantaneous observation in that season respectively. (For interpretation of the references to color in this figure legend, the reader is referred to the web version of this article.)

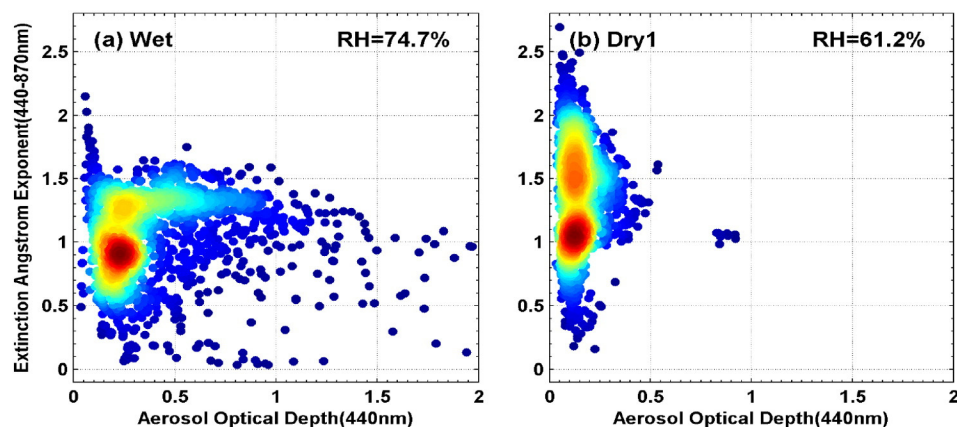


**Fig. 4.** The density plots of aerosol optical depth (AOD) vs. extinction Angstrom exponent (EAE) during the wet (May–October) and dry1 (November–February) seasons. The average values of daily relative humidity (RH) at KM from China Meteorological Administration are also shown here.

**Table 1**

Comparison of aerosol size parameters including volume mean radius ( $\mu\text{m}$ ), standard deviation, and volume concentration ( $\mu\text{m}^3/\mu\text{m}^2$ ) of total, fine, and coarse modes during the wet and dry1 seasons.

Size parameters	Wet season (May–September)			Dry1 season (Nov–Feb)		
	Total	Fine	Coarse	Total	Fine	Coarse
Volume mean radius	$1.10 \pm 0.50$	$0.18 \pm 0.05$	$3.27 \pm 0.60$	$1.01 \pm 0.49$	$0.15 \pm 0.02$	$3.23 \pm 0.31$
Standard deviation	$1.45 \pm 0.16$	$0.52 \pm 0.06$	$0.66 \pm 0.08$	$1.55 \pm 0.10$	$0.52 \pm 0.05$	$0.68 \pm 0.07$
Volume concentration	$0.16 \pm 0.07$	$0.07 \pm 0.05$	$0.09 \pm 0.04$	$0.06 \pm 0.04$	$0.03 \pm 0.03$	$0.03 \pm 0.02$

optical properties. First, the density plots of the instantaneous AOD as a function of EAE are compared between the wet and dry1 seasons. Second, the volume size distributions are binned by AOD and compared between wet and dry1 seasons. Third, the relationship between  $EAE_{440-870}$  and the spectral difference of EAE wavelength pairs ( $\delta_{EAE} = EAE_{440-675} - EAE_{675-870}$ ), an indicator to fine mode effective radius (Gobbi et al., 2007), is analyzed.

Aerosol types (UI, BB, dust/mixed dust) are analyzed according to the relationship of AAE and EAE following the method suggested by Mishra and Shibata (2012). The statistics of the occurrence of dominant aerosol types in different seasons are derived. The classification criteria are derived by summarizing the results of AAE for different aerosol types at typical AERONET stations (Mishra and Shibata, 2012). The classification criteria are as followed:  $EAE_{440-870} > 1.00$  and  $AAE_{440-870} > 1.20$  for BB;  $EAE_{440-870} > 1.00$  and  $0.70 < AAE_{440-870} < 1.30$  for UI; and  $EAE_{440-870} < 0.80$  and  $AAE_{440-870} > 1.30$  for dust aerosol. Black carbon coated by coarse particles such as dust and organic carbon is characterized by  $AAE_{440-870} < 1.0$  (Eck et al., 2010).

In addition to the analysis of aerosol types, further study of the aerosol loading and possible sources of aerosols on clean and polluted days is conducted using: (a) ground-based sunphotometer observation of daily AOD; (b) the mean MODIS\_AOD of both Terra and Aqua; and (c) 72-hour back-trajectory analysis at 2000 m a.s.l. using the Hybrid Single Particle Lagrangian Integrated Trajectory (HYSPLIT) model (Draxler et al., 1999). A case study of long-range transport of BB from North Burma to southwest China is performed using the CALIPSO total attenuated backscattering coefficient profiles at 532 nm, MODIS active fire products and back-trajectory analysis to reveal its significant impact on the column-integrated aerosol optical properties at KM.

### 3. Seasonal variation of aerosol optical properties and aerosol types

The monthly and seasonal statistics of aerosol optical properties observed by sunphotometer are presented in Fig. 3. The annual mean  $AOD_{440nm}$  at KM is  $0.42 \pm 0.32$ , which is much lower than observed

AOD at other urban areas of China. For example, the annual mean AOD at 550 nm is 0.77 in the Yangtze Delta region (Xia et al., 2007), 0.80 in the North China Plain (Li et al., 2007), and 0.92 at 533 nm over the Pearl River Delta (Ansmann et al., 2005). Distinct seasonal variability can be found for the AOD, EAE and CWV. The monthly mean  $AOD_{440nm}$  rapidly increases from 0.19 in February to 0.62 in March, then keeps relatively high values during the wet season and quickly decreases from 0.68 in September to 0.25 in October (the end of wet season) and continues to decrease to 0.15 in November (the first month of dry season). The seasonal mean  $AOD_{440nm}$ ,  $EAE_{440-870}$  and CWV amount during the wet season are respectively  $0.51 \pm 0.34$ ,  $1.06 \pm 0.34$  and  $4.25 \pm 0.97$  cm, which contrasts their counterparts during the dry1 season (November–February) of  $0.17 \pm 0.11$ ,  $1.40 \pm 0.31$  and  $1.91 \pm 0.37$  cm and dry2 season (March–April) of  $0.53 \pm 0.29$ ,  $1.39 \pm 0.19$ , and  $2.66 \pm 0.44$  cm. During the dry2 season (March and April, also the transition from dry to wet), AOD is the highest but CWV and particle size appears to be smaller than that of the wet season, which is likely related to BB that will be investigated in Section 4.

Larger values of CWV and AOD as well as smaller EAE (larger particles) during the wet season imply that the aerosol hygroscopic growth may have regulated the seasonal change of aerosol properties. In order to minimize the effect of variation of aerosol type on aerosol size, we only compare the aerosol properties in the wet and dry1 seasons as a function of RH to show the aerosol hygroscopic growth. The assumption is that aerosol types during these two periods change little. Fig. 4 illustrates the density plots between instantaneous  $AOD_{440nm}$  with  $EAE_{440-870}$  during the wet and dry1 seasons. The density centers of wet and dry1 season (in terms of AOD and EAE) are (0.25, 0.9) and (0.1–0.15, 1.0–1.1) and there is another center for dry1 season of (0.15, 1.5). The daily average values of RH from ground observation also show high in wet season and low in dry1. Thus, the much higher AODs and smaller EAEs (thereby larger particle size) are generally observed during the wet season compared to dry1 season, which is likely due to the aerosol hygroscopic growth. This finding is also revealed in the analysis of the aerosol size products as shown in Table 1. The volume

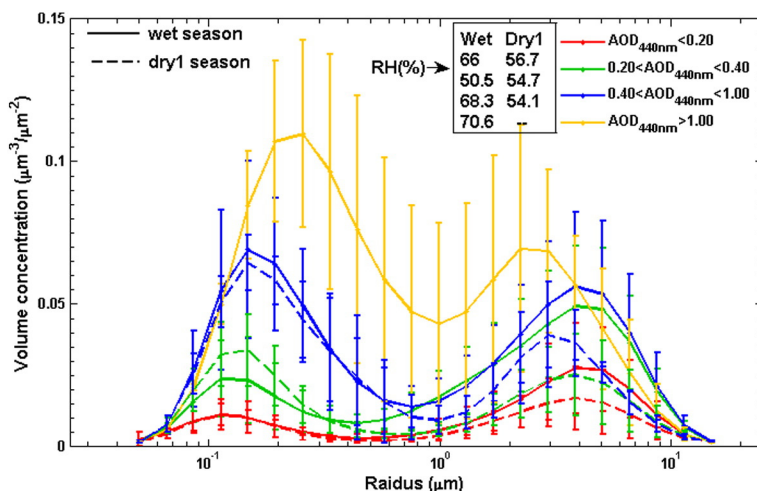
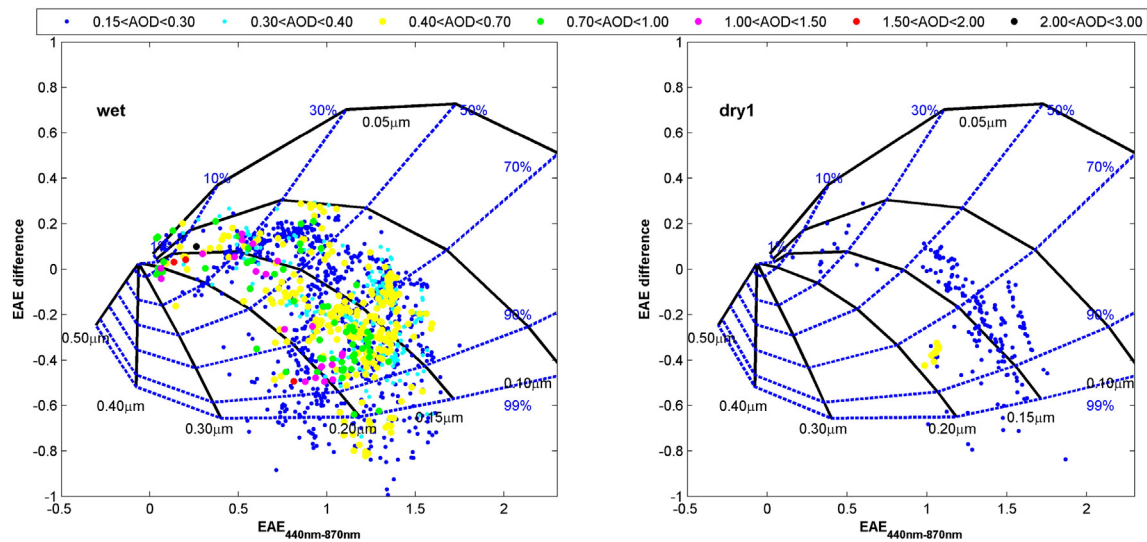


Fig. 5. The volume size distributions binned by AOD and the corresponding average of relative humidity (RH) in the wet and dry1 season.



**Fig. 6.** Extinction Angstrom exponent difference ( $\delta_{EAE}$ ), as a function of  $EAE_{440-870}$  and AOD during the wet and dry1 seasons. The solid lines represent a fixed radius of the fine mode, and the dashed lines are the fixed fraction ratio of fine mode to the total AOD. Only data with AOD > 0.15 are used. (For interpretation of the references to color in this figure legend, the reader is referred to the web version of this article.)

mean radius and the volume concentrations in wet season for fine and coarse aerosol modes are all larger than those in dry1 season. Furthermore, the aerosol effective radius in wet season is  $0.41 \pm 0.15 \mu\text{m}$ , ~30% larger than that during the dry1 season ( $0.33 \pm 0.12$ ).

To further analyze the contribution of the hygroscopic growth to the increase of aerosol size and thereby AOD, we stratify volume size distribution as a function of AOD for both the wet and dry1 seasons and the corresponding RH values are compared (Fig. 5). There are two interesting features. First, for both seasons, the volumes of both fine and coarse particles increase as AOD gets larger. However, the fine-mode volume shows a much larger relative increase (than coarse-mode) as a function of AOD, which suggests that AOD increase is largely due to fine mode particles. Second, the radius of the peak of fine mode during the wet season increases from  $0.11 \mu\text{m}$  for AOD < 0.20 to  $0.26 \mu\text{m}$  for AOD > 1.00. On the contrary, during the dry1 season, the peak radius varies little with AOD. Furthermore, except for AOD < 0.2 that represents the low aerosol loading, RH increases from 50.5% to 70.6% as AOD increases from 0.2–0.4 to more than 1.0 in wet season but RH appears stable (~55%) in dry1 season. Hence, the positive correlations of peak radius and volume of fine mode as well as AOD with RH in wet season suggest the possibility of hygroscopic growth of aerosol and its importance in regulating the change of aerosol properties.

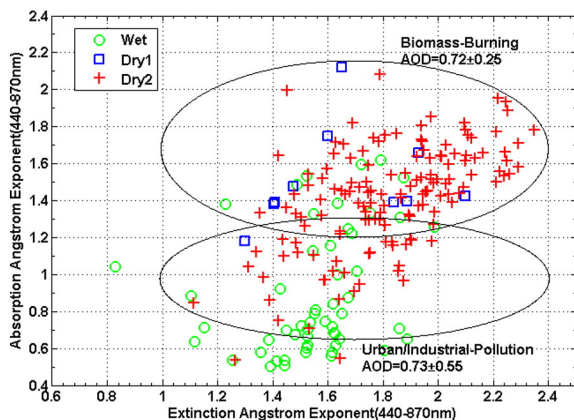


**Fig. 7.** Scatter plot of AAE vs. EAE, showing the clustering by aerosol type during the wet, dry1 and dry2 seasons.

To minimize the possibility of cloud contamination or the influence of the co-variation of coarse-mode and fine-mode aerosols in the analysis, we presented in Fig. 6 the scatter-plot of  $\delta_{EAE}$  and  $EAE_{440-870}$  binned by AOD during the wet and dry1 seasons. To avoid errors of  $\delta_{EAE}$ , only observations of AOD > 0.15 are used (Gobbi et al., 2007). Cloud contamination or an increase of the coarse mode fraction of AOD > 90% is normally characterized by zero values for both  $EAE_{440-870}$  and  $\delta_{EAE}$ . However, the increase of fine-mode AOD fraction, either due to the increase of fine-mode particle concentration, fine-mode particle radius, or both, will lead to an increase of  $EAE_{440-870}$  and negative  $\delta_{EAE}$  (as a result of a relatively larger increase in  $EAE_{675-870}$  than in  $EAE_{440-675}$  (Gobbi et al., 2007)). For AOD > 0.4 (yellow color in Fig. 6), we find: (a) the fine-mode aerosols size is generally less than  $0.15 \mu\text{m}$  during dry season, however, it is between  $0.15$  and  $0.2 \mu\text{m}$  in wet season; (b) a few cases during the wet season still show the similar fine-mode particle size like that of the dry season but AOD is dominated by large coarse-mode fraction (e.g., some yellow dots close to zero). While (b) likely reflects some potential in cloud contamination, cases for (a) are more dominant, which highlights the significance of the hygroscopic growth of the fine mode during the wet season and their significant effects on seasonal variation of aerosol optical properties.

Monthly mean  $SSA_{440nm}$  from March to October (late spring to fall) varies around ~0.89. A slight high value (~0.90) is found for  $SSA_{440nm}$  during the dry1 season, but interpretation here still requires further verification because retrievals of  $SSA_{440nm}$  in winter are very limited. Seasonal  $EAE_{440-870}$  during the wet season is  $0.93 \pm 0.32$ , smaller than that during the dry season ( $1.52 \pm 0.23$  for dry1 and  $1.34 \pm 0.24$  for dry2), which may be caused by aerosol hygroscopic growth (Day et al., 2000) or the aerosol type change (Bergstrom et al., 2002). AAE is a good indicator to aerosol types (Schnaiter et al., 2006; Bergstrom et al., 2007; Zhu et al., 2014), which can be used together with aerosol size to classify the dominant aerosol types or optical mixtures (Russell et al., 2010; Giles et al., 2011). Fig. 7 shows the scatter plot of instantaneous  $AAE_{440-870}$  and  $EAE_{440-870}$  during the different seasons. The results show that aerosols at KM can be classified into two major types: BB and UI. During the dry2 season, BB is the dominant component with a frequency of occurrence larger than 75%. During the wet season, UI aerosol dominates and its frequency is 40.7%; BB and AAE < 0.7 accounted for 24.7% and 40.6% respectively. The mean  $EAE_{440-870}$  of BB is  $1.85 \pm 0.24$  which is slightly larger than the UI ( $1.62 \pm 0.20$ ), suggesting the slightly smaller size of BB.

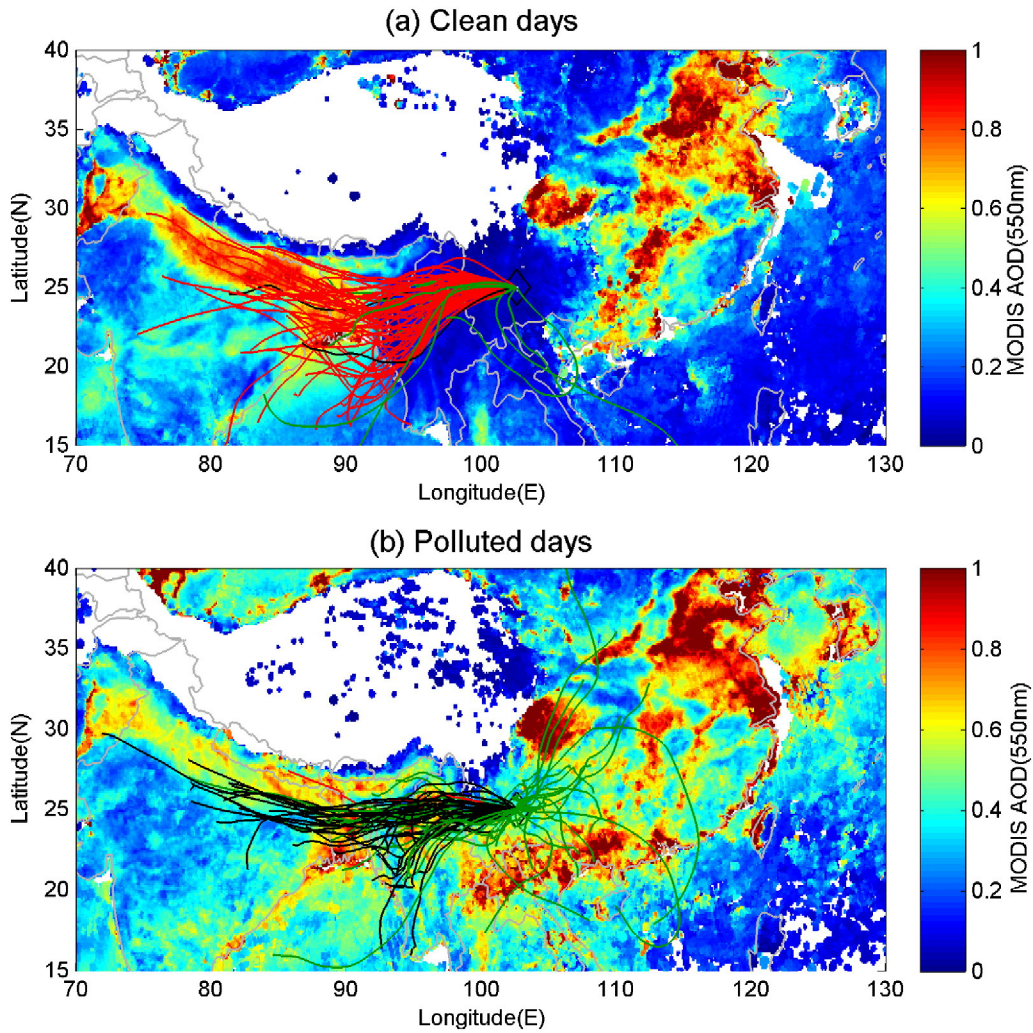


**Fig. 8.** The mean MODIS\_AOD and 72 h back trajectories at KM site during clean and polluted days. Green lines represent back trajectories on the day in wet season; red lines are back trajectories on the day during dry1 season and black lines are back trajectories on the day during dry2 season. (For interpretation of the references to color in this figure legend, the reader is referred to the web version of this article.)

**4. Comparison of airflows on clean/polluted days and long-range transport of BB aerosol**

In order to improve our understanding of seasonal AOD variation in southwest China, the analysis of the spatial distribution of MODIS\_AOD at 550 nm and airflows on clean and polluted days is performed, which

shows significant and interesting differences in air mass sources and regional distribution of MODIS\_AOD during the different seasons. The sunphotometer observations have been made over 300 days at KM. We sort the daily  $AOD_{440nm}$  in ascending order and select days with  $AOD_{440nm} < 25th\ percentile (AOD_{440nm} < 0.18)$  as clean day and days with  $AOD_{440nm} > 75th\ percentile (AOD_{440nm} > 0.58)$  as heavily polluted

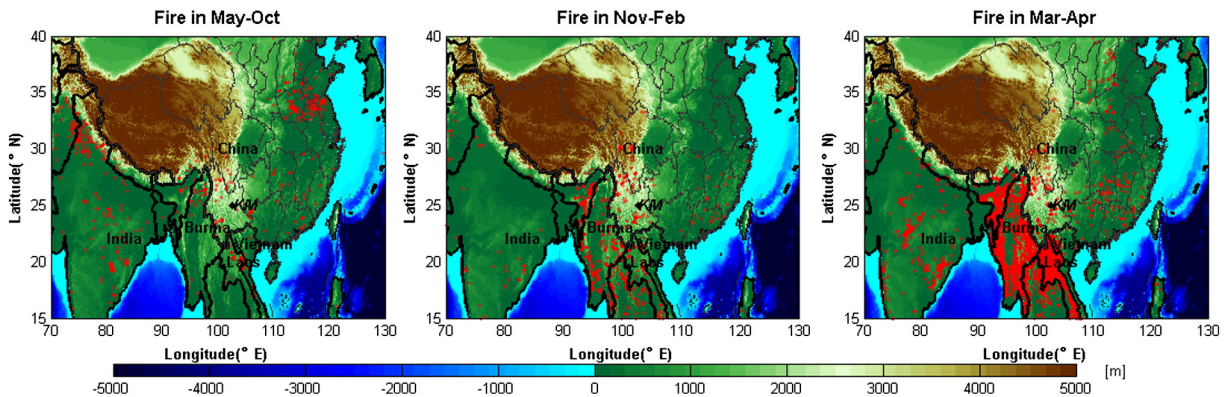


**Fig. 9.** MODIS fire points (red point) in the May–Oct (wet), Nov–Feb (dry1) and Mar–Apr (dry2) during the period of sunphotometer measurement (Mar 2012–Aug 2013). The topography of KM and surrounding area is also shown here. (For interpretation of the references to color in this figure legend, the reader is referred to the web version of this article.)

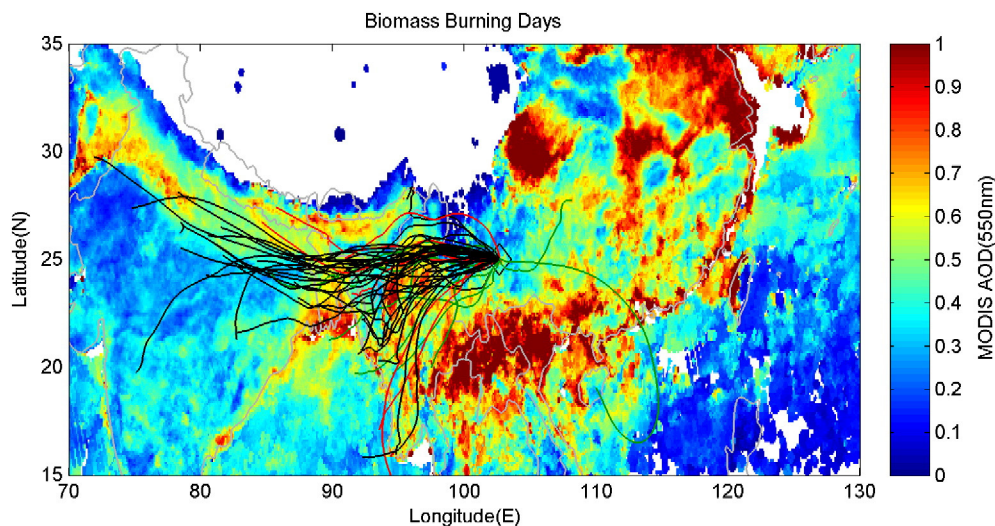


**Fig. 10.** The mean MODIS\_AOD and 72 h back trajectories at 2000 m a.s.l. on biomass burning polluted day. Green lines represent back trajectories on the day in wet season; red lines are back trajectories on the day during dry1 season and black lines are back trajectories on the day during dry2 season. (For interpretation of the references to color in this figure legend, the reader is referred to the web version of this article.)

day. So there are about 75 days for clean and polluted cases. The numbers of clean and polluted days are 14 and 42 for wet season, 61 and 1 for dry1 season and 2 and 32 for dry2 season. The polluted days in wet and dry2 seasons are mostly affected by UI and BB aerosol respectively.

A striking difference in the spatial MODIS\_AOD distribution and sources of airflows on clean and polluted days is shown in Fig. 8, the composite analysis of spatial distribution of MODIS\_AOD at 550 nm overlaid by 72 h back-trajectories ended at KM. There are a few interesting features on clean days. First, nearly all airflows are from the westerly direction except a couple of cases during the wet season that are characterized by southeast airflows. Second, most air masses are fast flowing according to the length of back trajectories. Third, a wide spread of MODIS\_AOD ( $<0.2$ ) is shown in southwest China and its surround areas that include North of Burma, Laos, and Vietnam. On the contrary, airflows on polluted days are quite different: (a) Although the dominant airflows during the dry2 season are also from the west, the moving speed is generally slow; (b) During the wet season, airflows arriving

at KM are mainly from the east and air mass sometimes stagnates around KM and its surrounding regions; (c) MODIS\_AOD in the upwind areas of KM during the wet season exceeds 0.4. The MODIS\_AOD in North Burma, an important upwind region of KM during the dry2 period, exceeds 0.6.

Fig. 9 shows the spatial distribution of fire counts detected by MODIS during the wet, dry1 and dry2 seasons. Comparing to the large increase in the number of fire counts over Southeast Asian countries in the dry2 season, the increase over Yunnan province is small. Given the prevailing westerly wind at KM, BB from Southeast Asia can be most likely transported to KM. Fig. 10 shows the mean MODIS\_AOD at 550 nm over 70–130°E and 10–40°N and 72 h back trajectories at KM on the days that BB aerosol observed. These events mainly occur in the dry2 season (the late dry season). The atmosphere is heavily polluted in the northern areas of Vietnam, Laos, and Burma, which is characterized by MODIS\_AOD of  $>0.6$  in Burma and  $\sim 1.0$  in Vietnam and Laos. The agriculture crop residue burning often occurs during this period, which causes a large spread of heavy aerosol pollution in source and

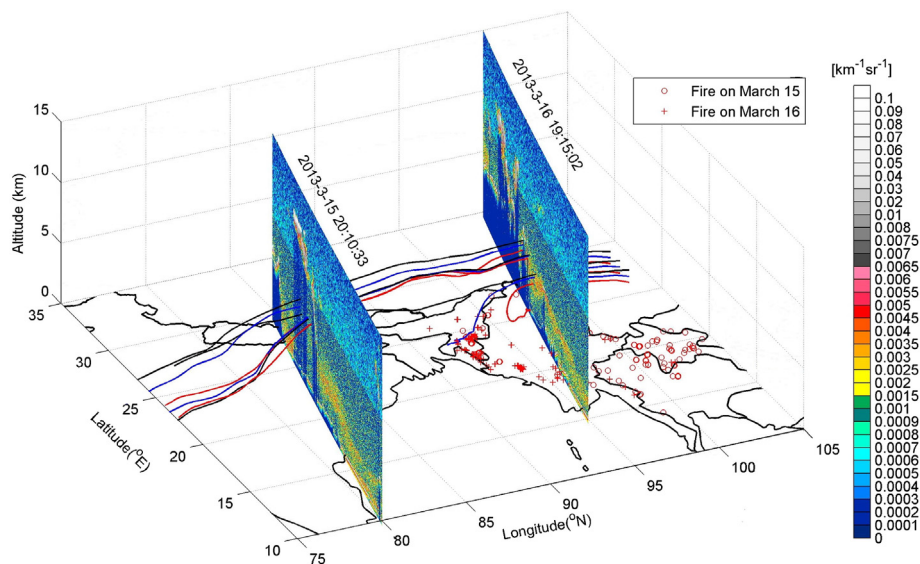


**Fig. 11.** Illustration of biomass burning aerosol transport during 15–17 March 2013. The red, blue, and black lines are 72 h back trajectories at three heights 2000 m, 2500 m and 3000 m ending at 00UTC on March 17 2013. The red markers are the fire locations on March 15 and 16. The vertical images (curtain files) show the CALIPSO 532-nm total attenuated backscatter ( $\text{km}^{-1} \text{sr}^{-1}$ ). (For interpretation of the references to color in this figure legend, the reader is referred to the web version of this article.)

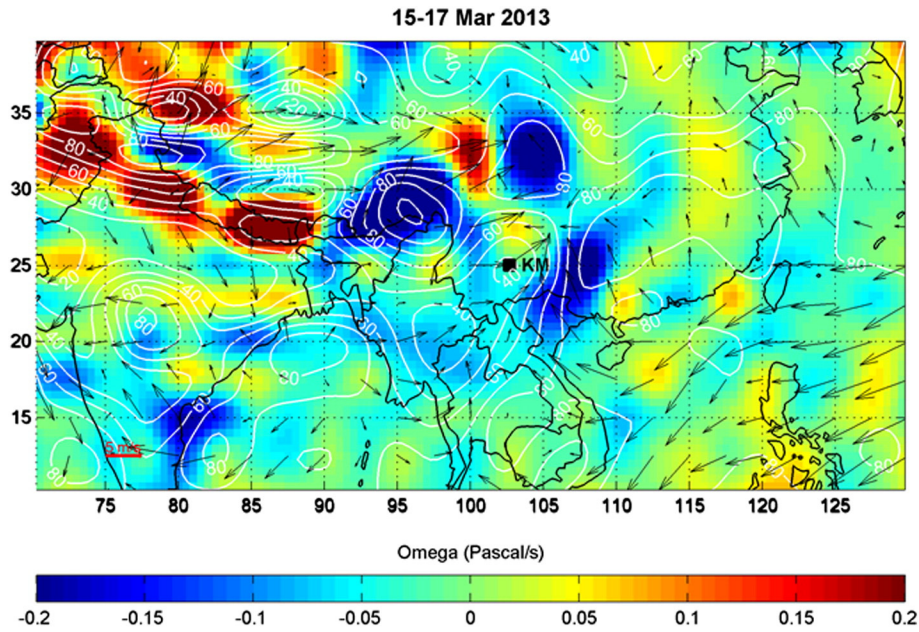


Fig. 12. The average surface wind, relative humidity (white line contour, %) and vertical velocity (Omega) during March 15–17 2013 from the NCEP/NCAR reanalysis data.

downwind regions (Deng et al., 2008). It is suggested by Fig. 10 that BB pollution at KM is likely associated with the long-range transport of BB aerosols by the prevailing westerly winds from North Burma, the up-wind region of KM.

To further analyze the transport of BB aerosols to KM, we studied one representative BB event occurred at KM (15–17 March, 2013) by using CALIOP profiling data and MODIS active fire products. The mean AOD, EAE, SSA, and AAE during these three days are 0.56, 1.61, 0.87, and 1.45, respectively. Fig. 11 illustrates the CALIOP attenuated backscatter curtains that are across North India on 15 March and North Burma on 16 March; also shown on Fig. 11 are the MODIS active fires and back trajectories. A wide spread of active fires is observed by the MODIS in the areas of northern Vietnam, Laos, and Burma. The thick aerosol layer as a result of BB is recorded by the CALIOP. The aerosol layer in North Burma extends from the surface to the height of ~ 5 km on the basis of the CALIOP measurement. Analysis of the vertical velocity (Omega) over the three days (Fig. 12), found that there was updraft over Burma (negative omega) and slight downdraft near KM, which

favored the long-transport of smoke aerosols in the source regions to the downwind regions. The thick smoke layer in North Burma is transported to the studied area by the prevailing westerly wind. On the contrary, BB in North Vietnam and Laos should play an insignificant role because the dominant air masses to KM are not originated at these areas although BB occurs there. Model study is needed for quantitative estimation of contribution of long-range transport of smoke aerosols to aerosol loading at KM.

### 5. Discussion and conclusions

Higher AODs are observed in the wet season at KM, which is different from many previous studies in the ITCZ-influenced regions that show low AOD during the wet season (Kaskaoutis et al., 2009). This is understood that in monsoon or ITCZ regions like south of India and some southeast Asian countries, precipitation occurs nearly every day during the wet season, washing out the aerosol in the air and allowing aerosol less time to grow. However, the climate at KM is different

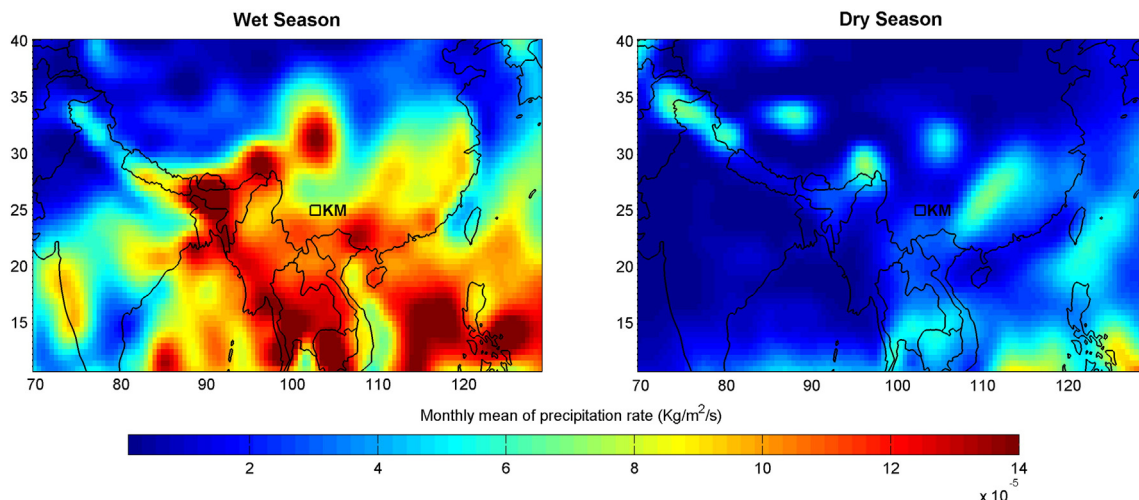


Fig. 13. The monthly precipitation rate during the wet and dry (including dry1 and dry2) seasons using the NCEP reanalysis monthly data during 2012–2013.

from that in the tropical ITCZ regions. Fig. 13 shows that the precipitation over KM during the wet season is much less than that of the tropical monsoon region. According to sunphotometer observations, the ratios of observation days to total days in the wet and dry seasons during the observation period are 0.45 and 0.79 respectively, which indirectly reflects that wet deposition process is not as significant at KM as that in other regions where wet season is affected by ITCZ. Nearly half of the wet season at KM is sunny so that aerosol hygroscopic growth is favored in high relative humidity environment that is revealed by the sunphotometer.

Using the CE318 sunphotometer data at KM, MODIS AOD and active fire products, CALIPSO aerosol profiles and the back-trajectories of HYSPLIT model, seasonal variability of aerosol optical properties, potential effects of the aerosol hygroscopic growth and long-range transport of BB aerosols on the study area are studied. The major conclusions are summarized as follows:

- (1) The annual means of the  $AOD_{440nm}$  and  $EAE_{440-870}$  during the observation period are  $0.42 \pm 0.32$  and  $1.25 \pm 0.35$ , respectively. Both parameters demonstrate a distinct monthly and seasonal variability. In comparison, AOD shows high values in wet ( $0.51 \pm 0.34$ ) and dry2 ( $0.53 \pm 0.29$ ) seasons but low in dry1 ( $0.17 \pm 0.11$ ) season, while EAE shows high values in dry1 ( $1.40 \pm 0.31$ ) and dry2 ( $1.39 \pm 0.19$ ) seasons but low in wet season ( $1.06 \pm 0.34$ ). High AOD, low EAE, larger effective radius, and distinct increase of fine mode aerosols with AOD and RH in the wet season suggest the importance of aerosol hygroscopic growth in regulating the seasonal change of aerosol properties at KM.
- (2) Quite different spatial distribution of MODIS\_AOD and air mass sources are observed for clean and polluted days. On clean days, the dominant airflows to KM are from the westerly direction during dry1 seasons, and a wide spread of low MODIS\_AODs ( $<0.2$ ) are observed in southwest China and its upwind regions. On polluted days, air masses are mainly from the west during the dry2 season and from the east during the wet season and high MODIS\_AODs ( $>0.4$ ) are observed in the upwind regions of KM.
- (3) The dominant aerosol type at KM is UI and BB aerosol. Frequent occurrences of BB aerosols at KM in March and April are closely associated with BB in North Burma. Analysis of one BB case shows that the smoke layer in the source regions can be transported to southwest China by uplifting and prevailing westerly winds.

## Acknowledgments

The authors are grateful to Haylie Mikulak of University of Nebraska-Lincoln for her help of proof-reading. This work is supported by Strategic Priority Research Program of the Chinese Academy of Sciences (XDA05100301), the National Science Foundation of China (41175031, 41375153) and the National Key Project of Basic Research (2014CB441201). The MODIS aerosol and active fire products are available from the Atmosphere Archive and Distribution System (LAADS) website (<http://ladswb.nascom.nasa.gov>) and the University of Maryland website (<ftp://fuoco.geog.umd.edu>), respectively. The CALIPSO data are from the Atmospheric Science Data Center (ASDC) website (<https://eosweb.larc.nasa.gov>). NCEP/NCAR Reanalysis data is downloaded from the Earth System Research Laboratory website (<http://www.esrl.noaa.gov/>).

## References

Ångström, A., 1929. On the atmospheric transmission of Sun radiation and on dust in the air. *Geogr. Ann.* 11, 156–166.

Ansmann, A., Engelmann, R., Althausen, D., Wandinger, U., Hu, M., Zhang, Y., He, Q., 2005. High aerosol load over the Pearl River Delta, China, observed with Raman lidar and Sun photometer. *Geophys. Res. Lett.* 32 (13).

Bergstrom, R.W., Russell, P.B., Hignett, P., 2002. Wavelength dependence of the absorption of black carbon particles: predictions and results from the TARFOX experiment and implications for the aerosol single scattering albedo. *J. Atmos. Sci.* 59 (3), 567–577.

Bergstrom, R.W., Pilewskie, P., Russell, P., Redemann, J., Bond, T., Quinn, P., Sierau, B., 2007. Spectral absorption properties of atmospheric aerosols. *Atmos. Chem. Phys.* 7 (23), 5937–5943.

Che, H.Z., Zhang, X.Y., Chen, H.B., Damiri, B., Goloub, P., Li, Z.Q., Zhang, X.C., Wei, Y., Zhou, H.G., Dong, F., Li, D.P., Zhou, T.M., 2009. Instrument calibration and aerosol optical depth validation of the China Aerosol Remote Sensing Network. *J. Geophys. Res.-Atmos.* 114 (D3).

Che, H., Xia, X., Zhu, J., Li, Z., Dubovik, O., Holben, B., Goloub, P., Chen, H., Estelles, V., Cuevas-Agulló, E., 2014. Column aerosol optical properties and aerosol radiative forcing during a serious haze-fog month over North China Plain in 2013 based on ground-based sunphotometer measurements. *Atmos. Chem. Phys.* 14 (4), 2125–2138.

Day, D.E., Malm, W.C., Kreidenweis, S.M., 2000. Aerosol light scattering measurements as a function of relative humidity. *J. Air Waste Manage. Assoc.* 50 (5), 710–716.

Deka, P., Hoque, R.R., 2014. Incremental effect of festive biomass burning on wintertime PM10 in Brahmaputra Valley of Northeast India. *Atmos. Res.* 143, 380–391.

Deng, X., Tie, X., Zhou, X., Wu, D., Zhong, L., Tan, H., Li, F., Huang, X., Bi, X., Deng, T., 2008. Effects of Southeast Asia biomass burning on aerosols and ozone concentrations over the Pearl River Delta (PRD) region. *Atmos. Environ.* 42 (36), 8493–8501.

Draxler, R.R., Stunder, B., Rolph, G., Taylor, A., 1999. HYSPLIT4 User's Guide. NOAA Technical Memorandum ERL ARL 230 p. 35.

Dubovik, O., King, M.D., 2000. A flexible inversion algorithm for retrieval of aerosol optical properties from Sun and sky radiance measurements. *J. Geophys. Res.* 105 (D16), 20673.

Dubovik, O., Smirnov, A., Holben, B.N., King, M.D., Kaufman, Y.J., Eck, T.F., Slutsker, I., 2000. Accuracy assessments of aerosol optical properties retrieved from Aerosol Robotic Network (AERONET) Sun and sky radiance measurements. *J. Geophys. Res.-Atmos.* 105 (D8), 9791–9806.

Dubovik, O., Holben, B., Eck, T.F., Smirnov, A., Kaufman, Y.J., King, M.D., Tanre, D., Slutsker, I., 2002. Variability of absorption and optical properties of key aerosol types observed in worldwide locations. *J. Atmos. Sci.* 59, 590–608.

Dubovik, O., Sinyuk, A., Lapyonok, T., Holben, B.N., Mishchenko, M., Yang, P., Eck, T.F., Volten, H., Muñoz, O., Veihelmann, B., van der Zande, W.J., Leon, J.F., Sorokin, M., Slutsker, I., 2006. Application of spheroidal models to account for aerosol particle nonsphericity in remote sensing of desert dust. *J. Geophys. Res.-Atmos.* 111 (D11).

Eck, T.F., Holben, B.N., Reid, J.S., Dubovik, O., Smirnov, A., O'Neill, N.T., Slutsker, I., Kinne, S., 1999. Wavelength dependence of the optical depth of biomass burning, urban, and desert dust aerosols. *J. Geophys. Res.* 104, 31,333–31,349.

Eck, T.F., Holben, B.N., Sinyuk, A., Pinker, R.T., Goloub, P., Chen, H., Chatenet, B., Li, Z., Singh, R.P., Tripathi, S.N., Reid, J.S., Giles, D.M., Dubovik, O., O'Neill, N.T., Smirnov, A., Wang, P., Xia, X., 2010. Climatological aspects of the optical properties of fine/coarse mode aerosol mixtures. *J. Geophys. Res.-Atmos.* 115.

Giglio, L., 2013. MODIS Collection 5 Active Fire Product User's Guide Version 2.5. [http://modis-fire.umd.edu/AF\\_usermanual.html](http://modis-fire.umd.edu/AF_usermanual.html).

Giles, D.M., Holben, B.N., Tripathi, S.N., Eck, T.F., Newcomb, W.W., Slutsker, I., Dickerson, R.R., Thompson, A.M., Mattoo, S., Wang, S.-H., Singh, R.P., Sinyuk, A., Schafer, J.S., 2011. Aerosol properties over the Indo-Gangetic Plain: a mesoscale perspective from the TIGERZ experiment. *J. Geophys. Res.* 116.

Gobbi, G.P., Kaufman, Y.J., Koren, I., Eck, T.F., 2007. Classification of aerosol properties derived from AERONET direct sun data. *Atmos. Chem. Phys.* 7, 453–458.

Hao, W.M., Liu, M.H., 1994. Spatial and temporal distribution of tropical biomass burning. *Glob. Biogeochem. Cycles* 8 (4), 495–503.

Holben, B.N., Eck, T.F., Slutsker, I., Tanre, D., Buis, J.P., Setzer, A., Vermote, E., Reagan, J.A., Kaufman, Y.J., Nakajima, T., Lavenu, F., Jankowiak, I., Smirnov, A., 1998. AERONET: a federated instrument network and data archive for aerosol characterization. *Remote Sens. Environ.* 66, 1–16.

Holben, B.N., Tanre, D., Smirnov, A., Eck, T.F., Slutsker, I., Abuhassan, N., Newcomb, W.W., Schafer, J.S., Chatenet, B., Lavenu, F., Kaufman, Y.J., Castle, J.V., Setzer, A., Markham, B., Clark, D., Frouin, R., Halthore, R., Karneli, A., O'Neill, N.T., Pietras, C., Pinker, R.T., Voss, K., Zibordi, G., 2001. An emerging ground-based aerosol climatology: aerosol optical depth from AERONET. *J. Geophys. Res.-Atmos.* 106 (D11), 12067–12097.

Huang, J., Minnis, P., Yi, Y., Tang, Q., Wang, X., Hu, Y., Liu, Z., Ayers, K., Trepte, C., Winker, D., 2007. Summer dust aerosols detected from CALIPSO over the Tibetan Plateau. *Geophys. Res. Lett.* 34 (18).

Jacob, D.J., Crawford, J.H., Kleb, M.M., Connors, V.S., Bendura, R.J., Raper, J.L., Sachse, G.W., Gille, J.C., Emmons, L., Heald, C.L., 2003. Transport and Chemical Evolution over the Pacific (TRACE-P) aircraft mission: design, execution, and first results. *J. Geophys. Res.-Atmos.* 108 (D20), 1–19.

Kalnay, E., Kanamitsu, M., Kistler, R., Collins, W., Deaven, D., Gandin, L., Iredell, M., Saha, S., White, G., Woollen, J., Zhu, Y., Chelliah, M., Ebisuzaki, W., Higgins, W., Janowiak, J., Mo, K.C., Ropelewski, C., Wang, J., Leetmaa, A., Reynolds, R., Jenne, R., Joseph, D., 1996. The NCEP/NCAR 40-year reanalysis project. *Bull. Am. Meteorol. Soc.* 77 (3), 437–471.

Kaskaoutis, D., Badarinarath, K., Kumar Kharol, S., Rani Sharma, A., Kambezidis, M., 2009. Variations in the aerosol optical properties and types over the tropical urban site of Hyderabad, India. *J. Geophys. Res.-Atmos.* 114 (D22).

Levy, R.C., Remer, L.A., Kleidman, R.G., Mattoo, S., Ichoku, C., Kahn, R., Eck, T., 2010. Global evaluation of the Collection 5 MODIS dark-target aerosol products over land. *Atmos. Chem. Phys.* 10 (21), 10399–10420.

Levy, R.C., Mattoo, S., Munchak, L.A., Remer, L.A., Sayer, A.M., Hsu, N.C., 2013. The Collection 6 MODIS aerosol products over land and ocean. *Atmos. Meas. Tech. Discuss.* 6 (1), 159–259.

Li, Z., Xia, X., Cribb, M., Mi, W., Holben, B., Wang, P., Chen, H., Tsay, S.C., Eck, T., Zhao, F., 2007. Aerosol optical properties and their radiative effects in northern China. *J. Geophys. Res.-Atmos.* 112 (D22).

- Li, Z., Li, C., Chen, H., Tsay, S.C., Holben, B., Huang, J., Li, B., Maring, H., Qian, Y., Shi, G., 2011. East Asian Studies of Tropospheric Aerosols and their Impact on Regional Climate (EAST-AIRC): an overview. *J. Geophys. Res.-Atmos.* 116 (D7).
- Luo, Y., Lu, D., Zhou, X., Li, W., He, Q., 2001. Characteristics of the spatial distribution and yearly variation of aerosol optical depth over China in last 30 years. *J. Geophys. Res.* 106, 14501–14514.
- Mishra, A.K., Shibata, T., 2012. Synergistic analyses of optical and microphysical properties of agricultural crop residue burning aerosols over the Indo-Gangetic Basin (IGB). *Atmos. Environ.* 57, 205–218.
- Qin, N., Chen, X., Fu, G., Zhai, J., Xue, X., 2010. Precipitation and temperature trends for the Southwest China: 1960–2007. *Hydrol. Process.* 24 (25), 3733–3744.
- Russell, P.B., Bergstrom, R.W., Shinozuka, Y., Clarke, A.D., DeCarlo, P.F., Jimenez, J.L., Livingston, J.M., Redemann, J., Dubovik, O., Strawa, A., 2010. Absorption Angstrom Exponent in AERONET and related data as an indicator of aerosol composition. *Atmos. Chem. Phys.* 10 (3), 1155–1169.
- Sahu, L.K., Saxena, P., 2015. High time and mass resolved PTR-TOF-MS measurements of VOCs at an urban site of India during winter: role of anthropogenic, biomass burning, biogenic and photochemical sources. *Atmos. Res.* 164, 84–94.
- Schnaiter, M., Gimmler, M., Llamas, I., Linke, C., Jäger, C., Mutschke, H., 2006. Strong spectral dependence of light absorption by organic carbon particles formed by propane combustion. *Atmos. Chem. Phys.* 6 (10), 2981–2990.
- Smirnov, A., Holben, B.N., Eck, T.F., Dubovik, O., Slutsker, I., 2000. Cloud-screening and quality control algorithms for the AERONET database. *Remote Sens. Environ.* 73 (3), 337–349.
- Streets, D.G., Yarber, K.F., Woo, J.H., Carmichael, G.R., 2003. Biomass burning in Asia: annual and seasonal estimates and atmospheric emissions. *Glob. Biogeochem. Cycles* 17 (4).
- Tao, R., Che, H., Chen, Q., Tao, J., Wang, Y., Sun, J., Wang, H., Zhang, X., 2013. Study of Aerosol Optical Properties Based on Ground Measurements over Sichuan Basin, China.
- Tao, R., Che, H., Chen, Q., Wang, Y., Sun, J., Zhang, X., Lu, S., Guo, J., Wang, H., Zhang, X., 2014. Development of an integrating sphere calibration method for Cimel sunphotometers in China aerosol remote sensing network. *Particology* 13, 88–99.
- Uchiyama, A., Yamazaki, A., Togawa, H., ASANO, J., 2005. Characteristics of Aeolian dust observed by sky-radiometer in the Intensive Observation Period 1 (IOP1). *J. Meteorol. Soc. Jpn.* 83, 291–305.
- Volz, F., 1965. Note on the global variation of stratospheric turbidity since the eruption of Agung Volcano. *Tellus* 17 (4), 513–515.
- Wang, L.L., Xin, J.Y., Li, X.R., Wang, Y.S., 2015. The variability of biomass burning and its influence on regional aerosol properties during the wheat harvest season in North China. *Atmos. Res.* 157, 153–163.
- Wehrli, C., 2005. GAW/PFR: a network of aerosol optical depth observations with precision filter radiometers. WMO/GAW Experts Workshop on a Global Surface-Based Network for Long Term Observations of Column Aerosol Optical Properties, p. 36.
- Winker, D.M., Pelon, J.R., McCormick, M.P., 2003. The CALIPSO mission: spaceborne lidar for observation of aerosols and clouds. Third International Asia-Pacific Environmental Remote Sensing Remote Sensing of the Atmosphere, Ocean, Environment, and Space. International Society for Optics and Photonics, pp. 1–11.
- Xia, X., Hong-Bin, C., Pu-Cai, W., Xue-Mei, Z., Jin-Huan, Q., Gouloub, P., 2005. Aerosol properties and their spatial and temporal variations over North China in spring 2001. *Tellus Ser. B* 57 (1).
- Xia, X., Li, Z., Holben, B., Wang, P., Eck, T., Chen, H., Cribb, M., Zhao, Y., 2007. Aerosol optical properties and radiative effects in the Yangtze Delta region of China. *J. Geophys. Res.-Atmos.* 112 (D22).
- Xia, X., Wang, P., Wang, Y., Li, Z., Xin, J., Liu, J., Chen, H., 2008. Aerosol optical depth over the Tibetan Plateau and its relation to aerosols over the Taklimakan Desert. *Geophys. Res. Lett.* 35 (16).
- Yan, H., Li, Q., Sun, C., Yuan, Y., Li, D., 2013. Criterion for determining the onset and end of the rainy season in Southwest China. *Chin. J. Atmos. Sci.* 37, 1111–1128.
- Zhang, Y.N., Zhang, Z.S., Chan, C.Y., Engling, G., Sang, X.F., Shi, S., Wang, X.M., 2012. Levoglucosan and carbonaceous species in the background aerosol of coastal south-east China: case study on transport of biomass burning smoke from the Philippines. *Environ. Sci. Pollut. Res.* 19 (1), 244–255.
- Zhao, H.M., Tong, D.Q., Gao, C.Y., Wang, G.P., 2015. Effect of dramatic land use change on gaseous pollutant emissions from biomass burning in Northeastern China. *Atmos. Res.* 153, 429–436.
- Zhu, J., Che, H., Xia, X., Chen, H., Goloub, P., Zhang, W., 2014. Column-integrated aerosol optical and physical properties at a regional background atmosphere in North China Plain. *Atmos. Environ.* 84, 54–64.